Design of a quadrotor flight test stand for system identification

M. M. Beharie
milanb@csir.co.za
UW-CSIR
Pretoria
South Africa

J. O. Pedro
jimoh.pedro@wits.ac.za
School of Mechanical, Industrial and Aeronautical Engineering
University of the Witwatersrand
Johannesburg
South Africa

L. Dala
ldala1@csir.co.za
UP-CSIR Aeronautics Chair
Pretoria
South Africa

ABSTRACT

This paper presents the design, development and construction of a flight test stand for a quadrotor UAV. As opposed to alternate forms of UAV, the power plant in the case of the quadrotor serves a dual purpose of control and propulsion. Since control and propulsion are coupled, the power plant (BLDC motor coupled with propeller) was studied in detail using a black box structure. Extractions of motor parameters in previous studies used traditional BLDC motor equations and propeller theory however the accuracy achievable and confidence in the extracted parameters remained questionable. The developed data acquisition process served to satisfy this need by the construction of a test bench that allows for the extraction of the unknown parameters instilling confidence in the modelling process. The established relationships are then used as inputs into a developed six degree of freedom Euler based mathematical model. A mission profile was constructed with distinct phases of which the mathematical model was used to simulate. Each phase in the mission profile excited different modes of the quadrotor dynamics creating an ideal simulation environment in which changes can be implemented and studied.

Paper No. 4037. Manuscript received 23 July 2013, revised version received 13 June 2014, accepted 21 October 2014.

https://doi.org/10.1017/S0001924000010587 Published online by Cambridge University Press

NOMENCLATURE

BLDC	brushless direct current (–)
b	beam width (m)
d_{perp}	lever arm length perpendicular to pivot point (m)
$F_{X_B}, F_{Y_B}, F_{Z_B}$	body-fixed forces (N)
g	gravitational acceleration (ms^{-2})
G_{Amp}	amplifier gain (–)
h	beam height (m)
K_v	kilo-volt (V)
l_{arm}	test bench arm length (m)
m	mass (kg)
mAh	milli-amp hour (A)
M_{TOTAL}	vehicle mass (kg)
$M_{X_B}, M_{X_B}, M_{X_B}$	body-fixed moments (N.m)
p,q,r	body-fixed angular rates (ms^{-2})
PWM	Pulse Width Modulation (–)
RPM	rotation rate in revolutions per a minute (s^{-1})
T	thrust force (N)
UAV	Unmanned Aerial Vehicle
u,v,w	body-fixed velocities (ms^{-1})
$\dot{u},\dot{v},\dot{w}$	body-fixed accelerations (ms^{-1})
$\vec{V}$	Volt (V)
V_{IN}	Amplifier Voltage supply (V)
V_{s+max}	switching voltage max (V)
V_{s+min}	switching voltage min (V)
V_{s-max}	switching voltage max (V)
V_{s-min}	switching voltage min (V)
$\mathbf{V}$	velocity vector (ms^{-1})
Ω	Angular rate vector (rad/s)

1.0 INTRODUCTION

The Unmanned Aerial Vehicle (UAV) is an aircraft with no pilot on board. They can be controlled remotely by an operator, or can be controlled autonomously via pre-programmed flight paths. Complex and risky missions without any on-board human involvement are the biggest advantage of UAV's. UAV's have attracted considerable interest for a variety of applications. Such aircraft have already been implemented by the military for reconnaissance flights, convoy protection, search and rescue operations and military attack missions. Future combat operations will continue to place unmanned aircraft in challenging conditions such as the urban warfare environment. However, the reduced autonomy and operator workload requirements of current unmanned vehicles present a roadblock to their success. It is anticipated that future operations will require multiple UAVs performing in a cooperative mode, sharing resources and complementing other air or ground assets. Surveillance and reconnaissance tasks that rely on UAVs require sophisticated modelling, planning and control technologies[1]. Civilian applications range from fire-fighting, site surveying, non-military security work, such as surveillance of pipelines, photography to meteorological work. While fixed-wing vehicles are suited for their range, speed and flight duration, rotorcraft or Vertical Take-Off and Landing (VTOL) vehicles are considered

https://doi.org/10.1017/S0001924000010587 Published online by Cambridge University Press

to be more preferable for surveillance, precise delivery and for missions requiring agility and accuracy. Control of the quadrotor is accomplished by varying the speeds of the four motors relative to each other. The four rotors present dual purposes as they are the sole sources of lift and the only form of control. Controlled flight of a quad-rotor would be virtually impossible by one operator, as the dynamics of such a system demand constant adjustment of four motors simultaneously. Having knowledge of the mapping between the speed of the motors, the lift produced by the propellers, the current consumed and the input signal allows for a better form of control technique to be adapted to the flight dynamics.

2.0 LITERATURE SURVEY

In the development of quadrotor UAV's, modelling, simulation and control have played a vital role[2,3,4]. The Control algorithms seek to provide robustness in the presence of uncertain parameters, unmodeled dynamics, external disturbances or failure situations[5,6]. When working with the unique design configuration of a quadrotor the underlying physic can be difficult to abstract and is an uncertain process. It is however of interest to reduce the amount of variables in the modelling situation through effective system identification methods deriving mathematical models from test data[7]. A case to be referred to in terms of modelling parameters of uncertainty is described by A. Raza and S. Etele[8] who developed a UAV test bench for the simulation environment to allow for testing potential techniques under realistic gust conditions. While there has been a lot of research done on the modelling of such a system with motor equations and blade aerodynamics[9], none have considered the development of an apparatus set and data sorting algorithm that has the capability of capturing the physical variation of the thrust vector with motor rating, blade pitch, blade diameter at a high level of repeatability. In contrast, Christiaan[10] used the technique of system identification to quantify the variation in thrust with RPM and through an analytical solver and ascertained the relationship for a single setup. Cheron[11] constructed a multifunction identification testbed for UAV actutators and used a real time MATLAB interface however did not consider these in a real time simulation. Stepaniak[9] studied the design of the electric propulsion system for a quadrotor by considering the characteristics of the motors combined with the speed controllers, variation in motor losses with frequency and the impact of heat dissipation with battery packs. This in turn allowed the optimisation of mission planning. Hoffman[13] evaluated the motor and rotor characteristics using a thrust test stand. It measures the forces and torques using a load cell with adjustable lever allowing for load sensitivity to be varied. An Atmel microprocessor board was programmed to perform motor control through its pulse width modulation (PWM) outputs, and to acquire analogue inputs from the load cell, current sensor, and battery voltage. The microprocessor board interfaces with a data acquisition program on the PC to perform automated tests, making measurements at 400 samples per second, well faster than the Nyquist frequency of the rotor rotation effects being measured. Oliveira[14] measured the torque generated by the motor of the quadrotor by placing its *Z*-axis perpendicular to the gravity vector effectively blocking the DOFs on the other axes.

3.0 RESEARCH RATIONALE

The low cost and simplicity of the quadrotor design provides an excellent testing ground for application of advanced system identification and control techniques which are ideally suited for research institutes and universities with small budgets. Prior to the design and build of the quadrotor, it is essential that a form of system identification is performed in order to ascertain the correct powerplant parameters. Identified powerplant parameters allow for simulations to be carried out, analysed and improved prior to costly construction.

https://doi.org/10.1017/S0001924000010587 Published online by Cambridge University Press

4.0 VEHICLE DYNAMICS

4.1 Mathematical modelling process

The flowchart illustrates the coupling of the moments and forces and is essential for debugging of the constructed mathematical model (see Fig.1). The relationship between torque, thrust, RPM and PWM were identified using a system identification technique and remain coupled due to the physical relationship that exist between parameters. Any change in rotor RPM is induced by a user defined input of PWM. The aforementioned quantities are utilised as input into the flight test bench. The model is constructed by initially evaluating the moments of inertia followed by the derivation of the equations of motion. The hub, gyroscopic rolling and pitching moments are then evaluated. Forces acting on the body in the form of thrust, drag and gravity are evaluated. The final equations of motion are then developed with a flight mission profile for real time analysis.

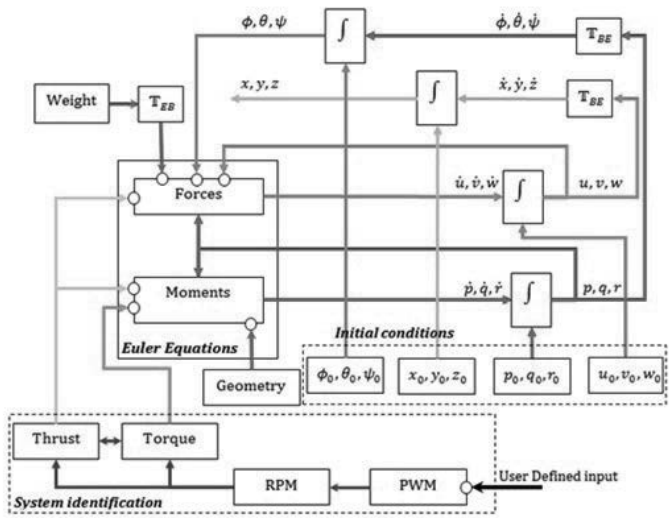


Figure 1. Flowchart of the mathematical modelling process.

4.2 Mathematical model

The mathematical model was created using Newton-Euler equations which required body and earth-fixed axes. The body-fixed axes allows for the inertias of the quadrotor to remain constant as opposed to variable inertias in an earth-fixed sense (see Fig. 2). The velocities and acceleration must be relative to an inertial frame of reference which is in the earth fixed frame. The attitude of the quadrotor is assessed by means of successive rotations around each one of the inertial axes, expressed in terms of the Euler roll, pitch and yaw angles. In order to simplify calculations it is better to consider the moments exerted on the quadrotor's airframe directly in the body-fixed rotating frame as assessing such a case in the earth fixed frame creates complexity due to constantly varying values as a function of time.

https://doi.org/10.1017/S0001924000010587 Published online by Cambridge University Press



Figure 2. Body-fixed axes attached to the quadrotor.

Expansion of Newton's second law for the translational dynamic gives:

$$\vec{F} = \frac{\delta(m.\vec{V})_{rot}}{\delta t} + \vec{\Omega} \times (m.\vec{V}) \qquad \ldots (1)$$

The matrix form of Equation (1) is given by Equations (2):

$$\begin{bmatrix} F_{X_B} \\ F_{Y_B} \\ F_{Z_B} \end{bmatrix} = M_{TOTAL} \begin{bmatrix} \dot{u} + qw - rv \\ \dot{v} + ru - wp \\ \dot{w} + pv - qu \end{bmatrix} \qquad \ldots (2)$$

The forces F_{X_b}, F_{Y_b} and F_{X_b} along the body fixed axes x, y and z axes are given by Equations (3), (4) and (5) respectively. $F_{X_{b-}}$, $F_{Y_{b-}}$ and $F_{X_{b-}}$ represent the reversal of the drag forces in the respective directions.

$$\sum F_{X_{B+}} x = -(m_{TOTAL} g)\mathrm{Sin}\theta + F_{D_{Bx}} \qquad \ldots (3(a))$$

$$\sum F_{X_{B-}} = -(m_{TOTAL} g)\mathrm{Sin}\theta + F_{D_{Bx}} \qquad \ldots (3(b))$$

$$\sum F_{Y_{B+}} = -(m_{TOTAL} g)\mathrm{Sin}\phi\mathrm{Cos}\theta + \left(F_{D_{By}}\right) \qquad \ldots (4(a))$$

$$\sum F_{Y_{B-}} = -(m_{TOTAL} g)\mathrm{Sin}\phi\mathrm{Cos}\theta + \left(F_{D_{By}}\right) \qquad \ldots (4(b))$$

https://doi.org/10.1017/S0001924000010587 Published online by Cambridge University Press

$$\sum F_{Z_B} = -(T_{rotor1} + T_{rotor2} + T_{rotor3} + T_{rotor4}) + \left(m_{TOTAL} g + F_{Drag}\right) \mathrm{Cos}\phi \mathrm{Cos}\theta \quad \ldots (5(a))$$

$$\sum F_{Z_{B-}} = -(T_{rotor1} + T_{rotor2} + T_{rotor3} + T_{rotor4}) + \left(m_{TOTAL} g + F_{Drag}\right) \mathrm{Cos}\phi \mathrm{Cos}\theta \quad \ldots (5(b))$$

The velocity along the body fixed axes are given by equating Equations (2) to (3), (4) and (5), then rearranging them to make the body fixed velocities the subject of formulae:

$$u = \int_{t=0}^{t=t} (vr - qw + g \ \mathrm{Sin}\,\theta).\mathrm{d}t + u_0 \quad \ldots (6)$$

$$v = \int_{t=0}^{t=t} (wp - ru + g \ \mathrm{Sin}\,\theta \ \mathrm{Cos}\,\theta).\mathrm{d}t + \upsilon_0 \quad \ldots (7)$$

$$w = \int_{t=0}^{t=t} (g \ \mathrm{Cos}\,\phi \ \mathrm{Cos}\,\theta - \frac{1}{M_{TOTAL}} (T_{total}) + qu - pv).\mathrm{d}t + \omega_0 \quad \ldots (8)$$

Application of Euler equations for the rotational dynamics is given by the following:

$$\vec{M} = \left(\frac{\bar{\mathrm{d}}\vec{L}}{\mathrm{d}t}\right)_{rot} + \vec{\Omega} \times \left(\vec{I}.\vec{\Omega}\right) \quad \ldots (9)$$

Where L represents the angular momentum and Ω the angular rate vector of the quadrotor in the earth fixed frame.
The scalar form of Equation (9) is given as:

$$\begin{bmatrix} M_{X_B} \\ M_{Y_B} \\ M_{Z_B} \end{bmatrix} = \begin{bmatrix} I_x \dot{p} + \left(I_x - I_y\right) qr \\ I_y \dot{q} + \left(I_x - I_z\right) rp \\ I_z \dot{r} + \left(I_x - I_z\right) pq \end{bmatrix} \quad \ldots (10)$$

Where:

I_x, I_y, I_z is the moment of the inertia about the x, y and z body fixed axes respectively.

Summing moments about the X_B (roll) axis:

$$\sum M_{X_B} \left(T_{Rotor1} - T_{Rotor3}\right) l_{arm} + I_G q \begin{bmatrix} -\omega_1 \\ +\omega_2 \\ -\omega_3 \\ +\omega_4 \end{bmatrix} \quad \ldots (11)$$

Similarly summing moment about the X_B (pitch) axis:

$$\sum M_{YT_B} \left(T_{Rotor4} - T_{Rotor2}\right) l_{arm} \quad \ldots (12)$$

https://doi.org/10.1017/S0001924000010587 Published online by Cambridge University Press

Similarly Equation (13) represents the summation of the moments about the Z_B axis.

$$\sum M_{Z_B}\left(T_{Rt4}-T_{Rt2}\right)-\left(T_{Rt3}-T_{Rt1}\right) \quad \ldots (13)$$

Where:

$T_{rotor1\text{-}4}$ is the thrust produced by motors 1-4 respectively.

$T_{R1\text{-}4}$ is the torque produced by motors 1-4 respectively.

The angular rates along the body fixed axes (p,q,r) are given by equating Equations (10) to (11), (12) and (13) then rearranging them to make the body fixed angular rates the subject of formulae: The pitch rate is given by:

$$p=\int_{t=0}^{t=t}\left(\frac{1}{I_x}\left(\left(T_{rotor1}-T_{rotor3}\right)l_{arm}+l_G q\begin{bmatrix}-\omega_1\\+\omega_2\\-\omega_3\\+\omega_4\end{bmatrix}+\left(I_y-I_x\right)gr\right)\right).dt \quad \ldots (14)$$

The roll rate is given by:

$$p=\int_{t=0}^{t=t}\left(\frac{1}{I_x}\left(\left(T_{rotor1}-T_{rotor3}\right)l_{arm}+l_G q\begin{bmatrix}-\omega_1\\+\omega_2\\-\omega_3\\+\omega_4\end{bmatrix}+\left(I_y-I_x\right)gr\right)\right).dt \quad \ldots (15)$$

The yaw rate is given by:

$$q=\int_{t=0}^{t=t}\left(\frac{1}{I_y}\left(\left(T_{rotor4}-T_{rotor2}\right)l_{arm}+\left(I_z-I_x\right)rp+l_G q\begin{bmatrix}-\omega_1\\+\omega_2\\-\omega_3\\+\omega_4\end{bmatrix}\right)\right).dt \quad \ldots (16)$$

4.3 Simulation model

The computer-based model realised in the Simulink environment allows for transparent graphical interfaces and various computational tools and parameters. The mathematical model in the Simulink environment had been broken up into the input, test bench(plant) and output as seen in Fig. 3. The input serves as actuators consisting of PWM signals where each PWM signal is individually actuated via a constant, step function or ramp function. RPM, torque and thrust are coupled functions of the PWM signal. The quadrotor model consists of the equations of motion of the system which determine the attitude of the vehicle when excited by the input. The output is composed of 12 quantities, the body-fixed velocities, body-fixed angular rates, angular position with respect to the earth-fixed axes and the position of the quadrotor within the earth-fixed axes.

https://doi.org/10.1017/S0001924000010587 Published online by Cambridge University Press

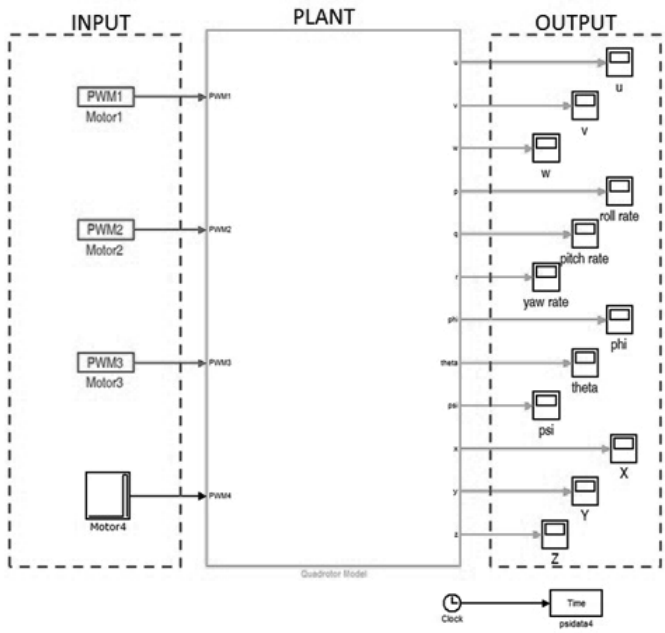


Figure 3. Simplified Simulink quadrotor motor representation.

5.0 DATA ACQUISITION PROCESS

The data acquisition phase remains an essential part of development for the Quadrotor control system as the inputs and outputs of the system play a vital role in the system identification process. As opposed to alternate forms of UAV, the power-plant in the case of the Quadrotor serves a dual purpose of control and propulsion. Since control and propulsion are coupled, it is essential that the power plant (BLDC motor coupled with propeller) is studied in detail. The data acquisition process serves to satisfy this need by the construction of a flight test bench that allows for the extraction of unknown parameters that define the control system. The parameters can be extracted using BLDC motor equations and propeller theory however the accuracy achievable and confidence in the data remains questionable. A black box structure was implemented on the powerplant in order to extract

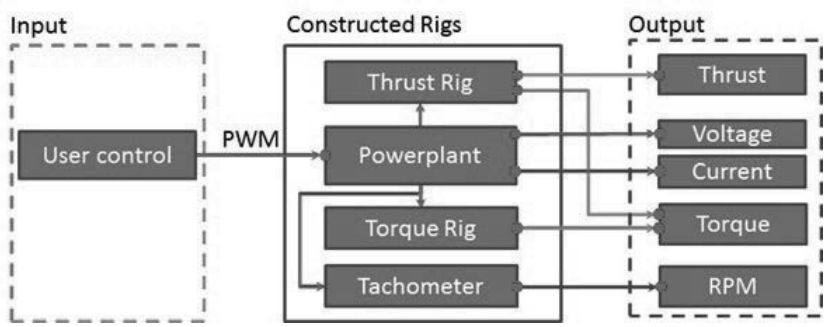


Figure 4. Overview of the data acquisition process.

https://doi.org/10.1017/S0001924000010587 Published online by Cambridge University Press

the thrust, voltage, current, torque and RPM values. Relationship between these variables were then made allowing for a more realistic mathematical modelling of the system. Figure 4 illustrates the overview of the data acquisition process with the constructed hardware and output signals.

5.1 Thrust test rig

The physical differences in construction of BLDC motors make the performance of each motor unique. These differences affect the performance of the motor, amplifying the need for an apparatus that allows for performance specification to be extracted for a variation in propeller profiles. This need was satisfied by the construction of a custom built load cell as seen in Fig. 5. The load cell incorporated strain gauges mounted on the top base and bottom of the cantilever beam to complete a full bridge strain gauge setup increasing the resolution. The deflection of the beam creates a change in beam length which translates to a change in strain gauge length. This increases the resistance of the strain gauge pair unbalancing the bridge. A minimum of two strain gauges (2 or 4 gage system) were used as one needed to be in compression whilst the other in tension. Equation (17) illustrates the relationship between the strain gauge amplifier gain, beam geometry, material properties, thrust force and excitation voltage. This allows for the design of the beam to be optimised operating within a limit load.

$$V_{OUT} = \left(\frac{12 F_{thrush} L}{b h^2 E} \right) V_{IN} G_{Amp} \quad \ldots (17)$$

Two vertical beam mounts were used to isolate beam motion in the vertical plane whilst ensuring the fixed-free beam end conditions. This was further enforced by a pair of three hexagonal bolts serving as claps along the y and x-axis. The bolts further allowed for a variation in beam length and height.

5.2 Torque test rig

Motor torque is measured via leverage system which when coupled to the thrust rig allows for a variation in torque with RPM to be captured. Isolation of the motor in this position allows for a single degree of freedom about the bearing axis which represents the pivot point as Fig. 6. The torque rig was created using the fundamental definition of torque as described by Equation (18):

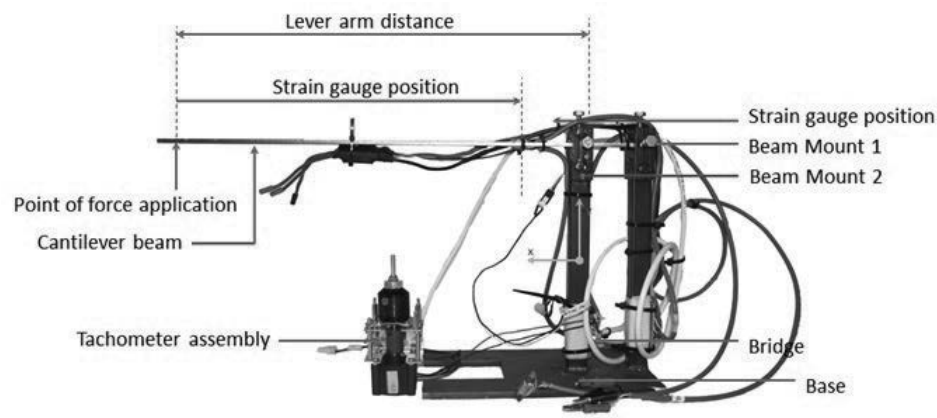


Figure 5. Constructed thrust test rig.

https://doi.org/10.1017/S0001924000010587 Published online by Cambridge University Press

$$\text{Torque} = Td_{perp} \quad \ldots (18)$$

Torque can be calculated by the use of a lever arm combined with the component of the force perpendicular to the lever arm. The force in the case of the torque rig is generated by the rotation of the BLDC motor and drag penalty.

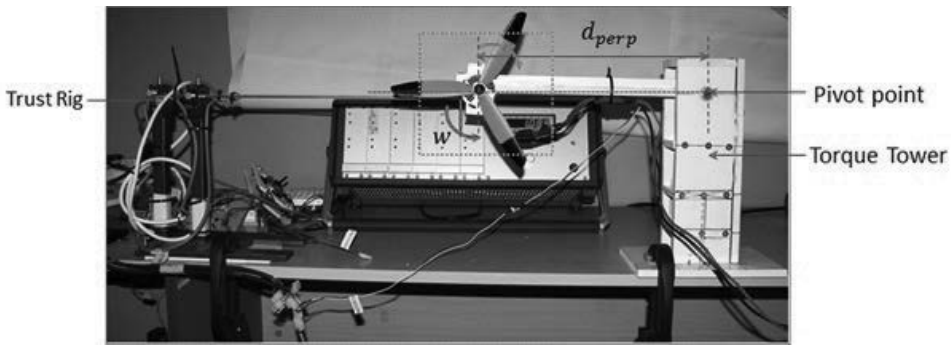


Figure 6. Constructed torque test rig.

The torque rig as presented in Fig. 6 was constructed from expanded foam sheeting due to the ease of construction. The four tier structure was created for added height and the cubicle construction for rigidity compensating for the added bending moment induced by the thrust force generated by the blades. The forces acting on the arm of the thrust tower are bi-planar; there exist a thrust force generated by the blades which are reacted upon by the moment generated by the clamping force on the base and the bearing support.

5.3 Current monitoring

The monitoring of current consumed by the motor is important in establishing a rough estimate on the range and endurance of the Quadrotor. Brushless DC Motor Rating is generally provided in KV. The Kilo-Volt(KV) rating in brushless motors refers to the amount of revolutions that can be achieved per a volt. Capacity indicates how much power the battery pack can hold and is indicated in milliamp hours (mAh). In simpler terms, it signifies the maximum amount of current that can be drawn in an hour duration for the battery to fully discharged. Capacity indicates how much power the battery pack can hold and is indicated in milliamp hours (mAh). In simpler terms, it signifies the maximum amount of current that can be drawn in an hour duration for the battery to fully discharged.

5.4 RPM monitoring

RPM monitoring is an essential parameter in establishing an accurate motor performance prediction. The constructed propeller RPM encoder illustrated in Fig. 7 consists of two horizontal plates forming the mounting platforms for the IR NPN Phototransistor (SFH300) and transmitter (SFH-484) on the vertical metal tubing. Mounting the receiver on the upper platform avoids any possible infrared light wave interference from non-natural lighting (Fluorescent globes emit IR). The variability in the interrupt distance is an important feature as at higher RPM blade flutter

https://doi.org/10.1017/S0001924000010587 Published online by Cambridge University Press

becomes more prominent. The functioning of the encoder is dependent on the obstruction of the infrared pathway registering a Boolean value. In the case of the tests performed, the spinning propeller provides the necessary obstruction. The non-contact RPM sensor is advantageous in that it allows for RPM to be measured without the losses associated with a direct coupling tachometer on the motor drive.

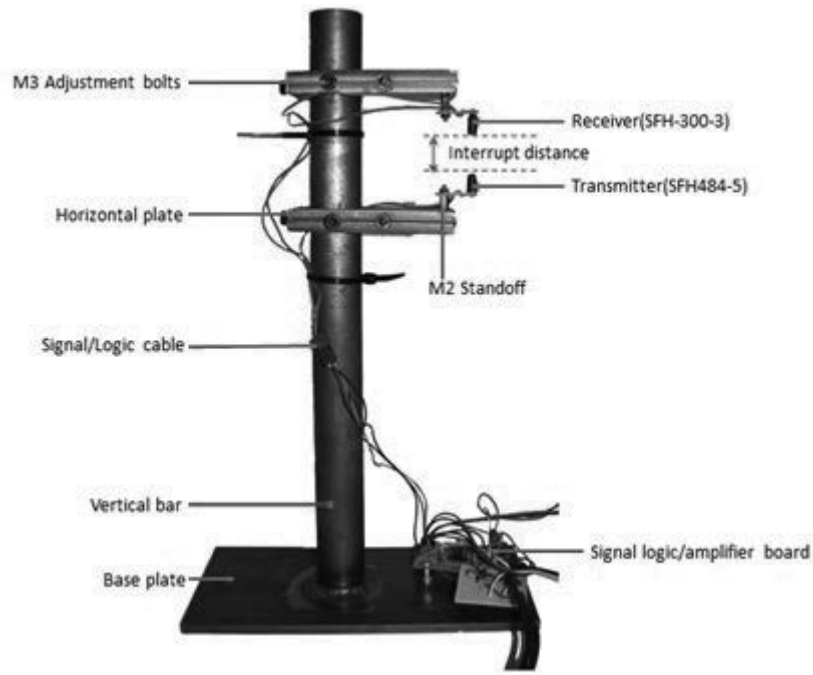


Figure 7. Constructed torque test rig.

The receiver and transmitter were paired using the peak sensitivity values. The phototransistor and transmitter have a peak sensitivity of 850nm and 880nm respectively. NPN-phototransistor with its emitter connected to ground has a voltage that varies depending on the wavelength of light entering the transistor. The value of current that is output from the receiver is measured post setup allowing for a distinct point at which the Schmitt trigger can switch to a high voltage (5V) and low voltage (0V). The distinct switching point facilitates easier data capture for controllers.

6.0 IDENTIFICATION RESULTS

6.1 Motor performance results

Avoiding errors whilst maintaining consistency involved the collection of multiple data sets for each test run. Motor benchmarking involved the testing of seven motors combined with six propeller types. The seven motors ranged from 390KV to 1,200KV. The 390KV, 490KV, 570KV and 690KV consisted of a 22 pole arrangement as opposed to the remaining 12 pole arrangement of the 850KV, 1,000KV and 1,250KV arrangements.

https://doi.org/10.1017/S0001924000010587 Published online by Cambridge University Press

Table 1
Motor rating and pole arrangement

Motor Power rating(KV)	Poles
390, 490, 570, 690	22
850, 1,000, 1,250	12

The 850KV motor failed to function after two runs and was neglected from the testing schedule. Each data set consisted of 6,000 data points making the processing of these curves cumbersome. The developed data sorting algorithm allowed for the raw data points to be minimised to 19, each data point along a constant PWM step input. Figure 8 illustrates the reduction of data point through the data processing phase. The raw data consisted of torque, thrust, RPM and PWM all of functions of time.

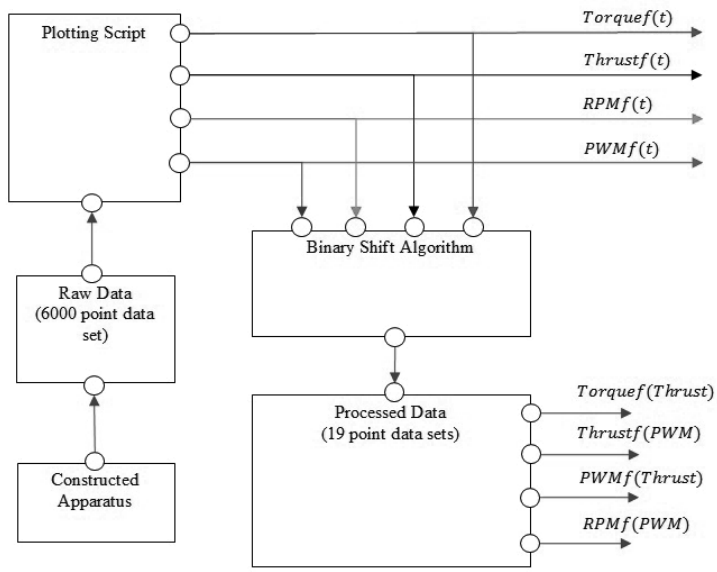


Figure 8. Overview the data processing and presentation process.

The two quantities that are of main interest during motor selection:

- Motor current consumption: This is vital in determining the range of the quadrotor and directly impacts the mission profile selection.
- Variation in RPM with Thrust and PWM: This is vital in control and simulation as a direct mapping allows for more precise and effective control algorithms to be developed via the feedback provided via encoders.
- Maximum thrust value: This directly impacts the payload capability of the quadrotor.

The variation in the above quantities with motor and propeller type can be viewed in Fig. 9 and Fig. 10 respectively. The figures indicate that the smaller KV motors produce less thrust than the higher KV counterparts and also consumes less current. The highest thrust value of 675 grams was produced by the 1,000KV motor combined with a 11 × 4·5″ blade drawing 15·64 amps of current.

https://doi.org/10.1017/S0001924000010587 Published online by Cambridge University Press

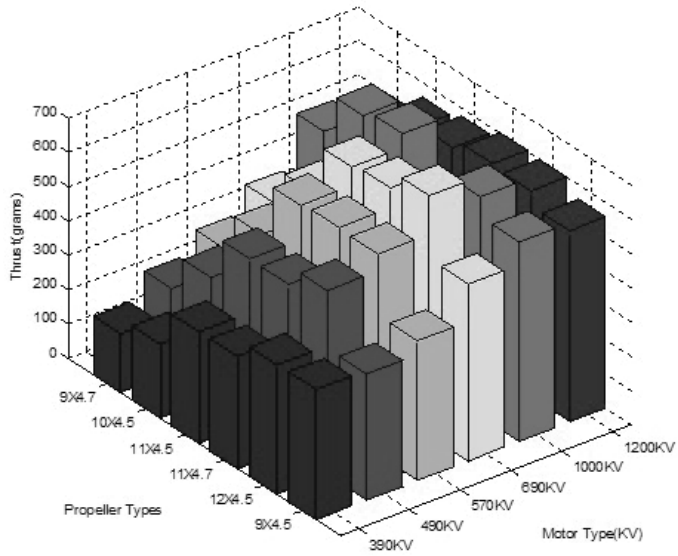


Figure 9. Thrust variation for all test runs.

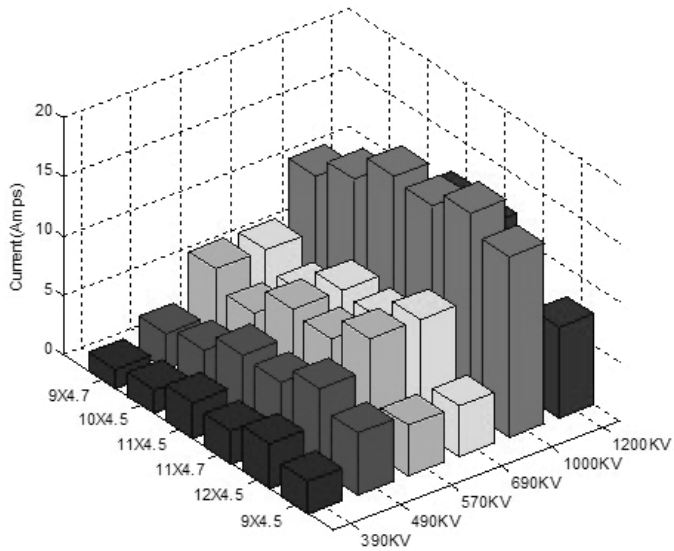


Figure 10. Current variation for all test runs.

The lowest thrust value of 171 grams was produced by the 390KV motor combined with a $9 \times 4{\cdot}7''$ blade drawing 1·61A of current. The above mentioned motors set the upper and lower limit for performance and endurance however a compromise between the two criteria are essential. A solution that satisfies both criteria can be found by studying the effect of current and thrust jointly. Figure 11 was created by dividing the maximum thrust produced by each motor with the current consumption at the recorded thrust value (Equation (19)).

https://doi.org/10.1017/S0001924000010587 Published online by Cambridge University Press

$$Efficiency = \frac{Max\ Thrust}{Current} \quad \ldots (19)$$

In a physical sense this translates to the amount of thrust produced by the motor in grams per unit amp. This can be interpreted as the efficiency of the motor, as the current drawn by the motor can be considered as an input and the thrust generated by the powerplant as an output.

Figure 10 illustrates the variation in the thrust per unit current with propeller and motor type. The absence of a result for the 12 × 4·5″ propeller combination with the 1,200KV motor is a result of the inability of the motor to turn the larger diameter£$ propeller. The lower KV motors produce more torque due to the higher pole count allowing for a higher starting torque overcoming the higher inertia value of larger blade diameters. Further assessing Fig. 11 , it can be deduced that the highest conversion of current to thrust increases with the decrease in motor KV. This is represented by the higher dark blue and light blue peaks of the 390KV and 490KV motors. The 390KV motor combined with the 9 × 4·5″ three blade propeller produces the highest ratio of thrust to current and would be the motor of choice but does have a limitation. The highest thrust to current ratio does not imply a higher overall thrust in the numerator of the ratio (see Equation 19) but can imply a smaller denominator creating a larger value and in the case of the 390KV motor the maximum thrust is the lowest of all the motors. In order to overcome this problem, a proposed mass of the quadrotor(1·3kg) was used. Additionally during ascend and forward flight a resultant thrust is needed to overcome the weight of the UAV and still have the additional capacity to accelerate the craft. In order for this requirement to be met the maximum thrust needed was set to 19·62N (2g).

7.0 SIMULATION RESULTS

The Simulink model used four different control inputs to generate four modes of flight. Each mode exciting the vehicle dynamics making for a quantifiable analysis on which stabilty can be jugdged. The state of the PWM signals, displacements, velocities and trajectories serve as visual reperesentation of essential telemetry that can be used to determine atitude.

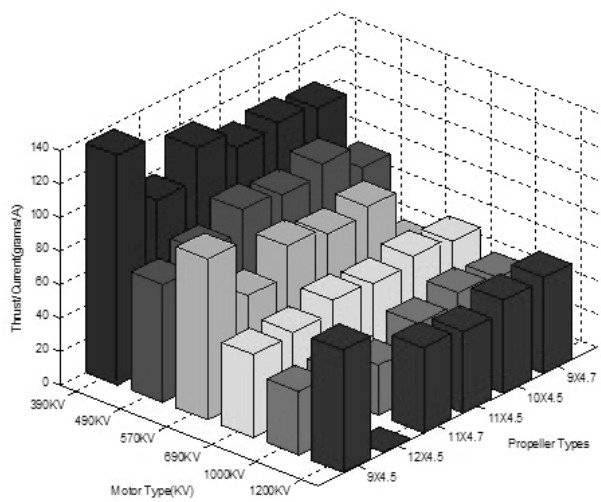


Figure 11. Comparative analysis of all tested motors.

https://doi.org/10.1017/S0001924000010587 Published online by Cambridge University Press

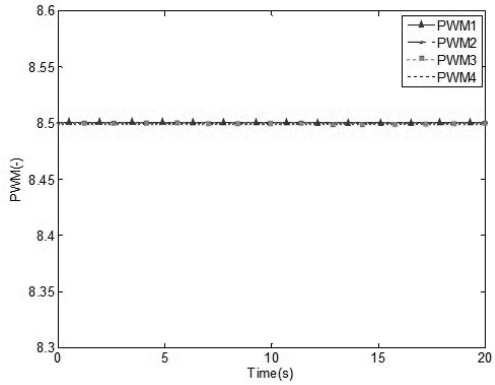


Figure 12. PWM signal for all motors during the ascent phase.

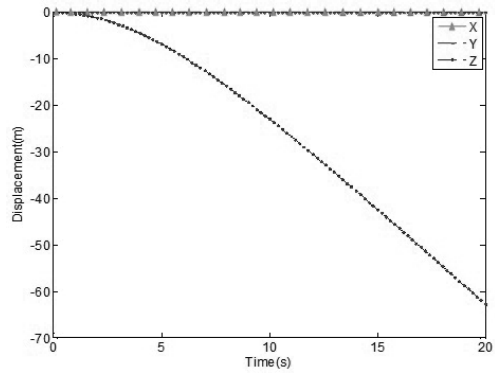


Figure 13. Variation in displacement with time during the ascent phase.

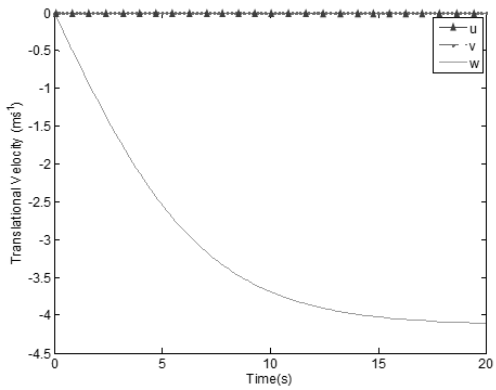


Figure 14. Variation in translational velocity with time during the ascent phase.

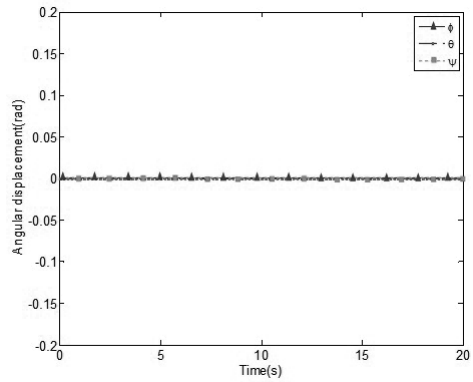


Figure 15. Variation in angular displacements with time during the ascent phase.

7.1 Take-off/ascent phase

The first control input consisted of a constant PWM mode in the ascent phase. To initiate a take-off sequence the motors need to receive a PWM signal higher in magnitude than that at the equilibrium phase. A PWM signal of 8·5 was generated on each motor channel as seen in Fig. 12. During the take off phase the quadrotor climbs 63m in 20s at a PWM input of 8·5 with the body fixed and earth fixed axis being aligned. The resultant force is a function of the thrust, weight of the quadrotor and drag force A null resultant force is the effect of the drag vector against the motion of the quadrotor which can be seen in Fig. 13 and Fig. 14 and, where the translational velocity plateau's to a value of $4ms^{-1}$ implying a constant velocity and the displacment curve gradient remains constant. Angular rates and displacements (seen in Fig. 15 and Fig. 16) are null due to a balance in moments generated by each pair of thrust forces and a singular resultant force along the *z*-axis of the earth. Figure 17 illustrates the take-off trajectory on the earth fixed axis. These results ascertain the functioning of the model with emphasis being placed on the drag components in each direction. Take-off was initiated from sea level.

https://doi.org/10.1017/S0001924000010587 Published online by Cambridge University Press

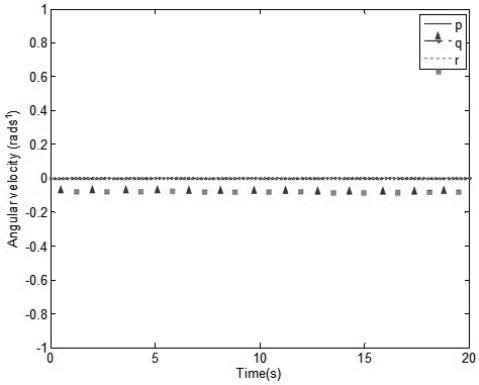


Figure 16. Variation in angular velocity with time during the ascent phase.

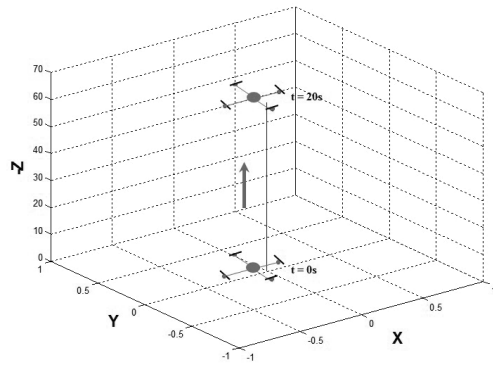


Figure 17. Trajectory plot during the ascent phase from base.

7.2 Hover phase

The hover phase follows the take-off phase and involves the quadrotor holding its altitude. Figure 19 is the illustrative of this as there is no variation in the X, Y and Z co-ordinates with time. The position of the quadrotor with time remains at the co-ordinate achieved post take-off as previously illustrated in Fig. 17. This requires the equilibrium PWM signal to be generated by each motor as seen in Fig. 18. The resultant force in the body-fixed frame is null implying an equilibrium condition. Translational and angular rates are null as seen in Fig. 20, Fig. 21 and Fig. 22 respectively. Control is not essential at this phase of the mission due to the absence of dynamic environmental conditions and absence of rotational rates which generate a resultant force on the body frame.

7.3 Mode excitation phase

The mathematical model of the quadorotor system as described earlier consists of second order differential equations creating a challenging stability analysis. Figure 23 illustrates the the system being excited by the generation of three constant PWM signals and a fourth ramp/step

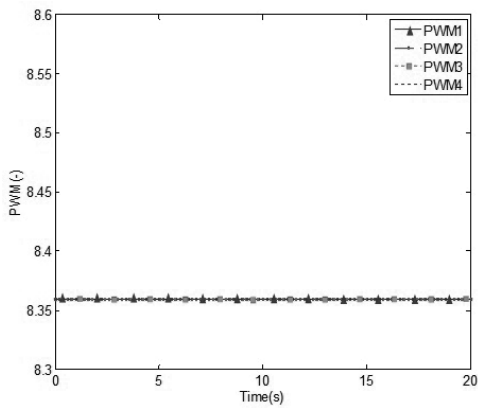


Figure 18. PWM signal for all motors during the hover phase.

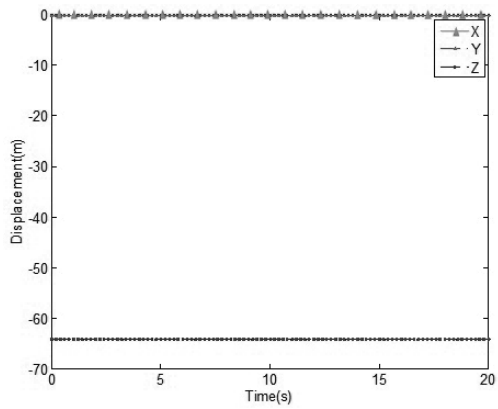


Figure 19. Variation in displacement with time during the hover phase.

https://doi.org/10.1017/S0001924000010587 Published online by Cambridge University Press

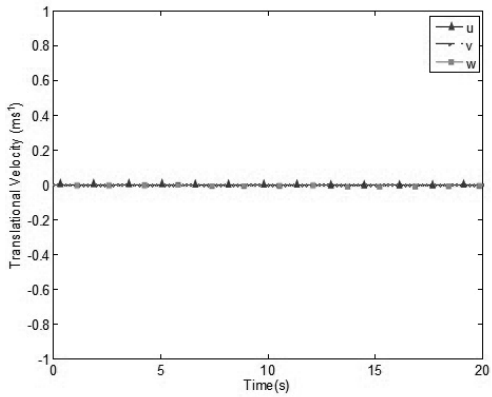


Figure 20. Variation in the translational velocity with time in the hover phase.

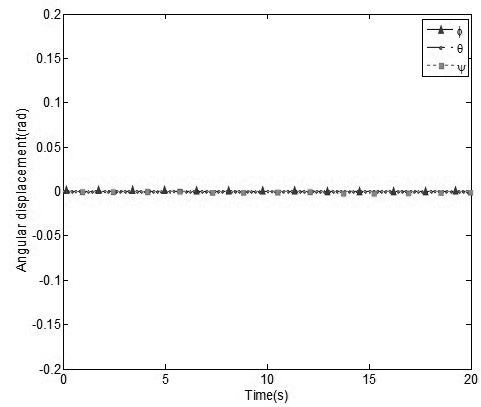


Figure 21. Variation in angular displacements with time during the hover phase.

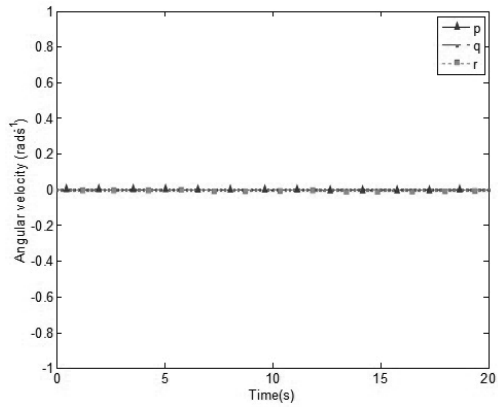


Figure 22. Variation in angular velocity with time during the hover phase.

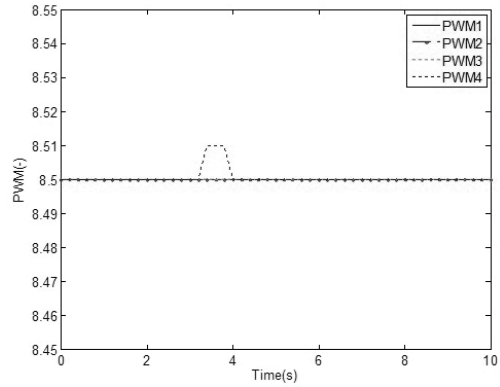


Figure 23. PWM signal for all motors during a signal perturbation on motor four.

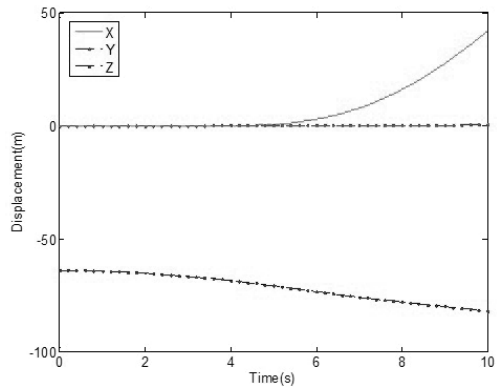


Figure 24. Variation in the displacement with time in the excitation phase.

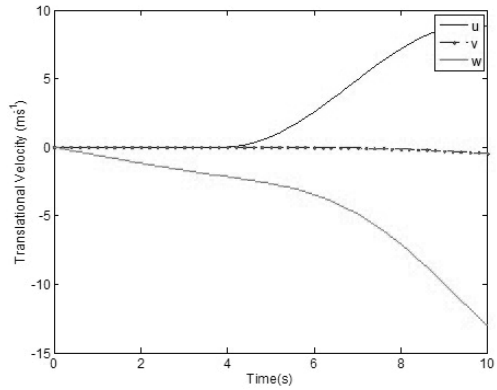


Figure 25. Variation in the linear velocity with time in the excitation phase.

https://doi.org/10.1017/S0001924000010587 Published online by Cambridge University Press

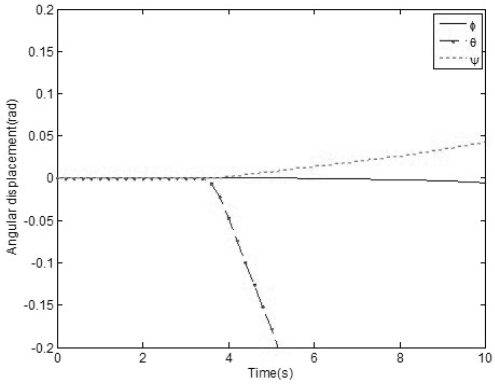


Figure 26. Variation in the angular displacement with time in the excitation phase.

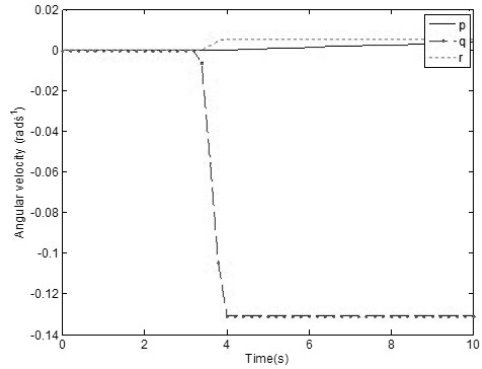


Figure 27. Variation in the linear velocity with time in the excitation phase.

function. The simulation is intiated at an altitude of 63 meters with a simulation end condition of 0 meters above sea level. The step function initially holds a PWM value of 8·5 which is then increased to a value of PWM = 8·51 for 0·15 second after which it returns to the initial value of PWM = 8·5. It can be noted by observing Fig. 25 that the pulsed PWM signal sent to motor four creates a rolling moment. This increases the pitch angle as in Fig. 26 changing altitude and increasing the translational velocity. The change in PWM signal on rotor four induces an additional yawing moment as seen in Fig. 26 and Fig. 27 changing the X co-ordinate with time resulting a curved flight path as seen in Fig. 28.

7.3 Landing/descent phase

The final phase of the mission profile consists of the descent phase. This phase is similar to the ascent phase in that the PWM signals generated for the motors are constant however at a PWM signal lower than that required to maintain hover (see Fig. 29). The PWM signal supplied for the purposes of testing was set to a value that allowed for a steady landing. During this phase the displacement occurs only along the earth-fixed Z-axis and due to the drag vector the displacement

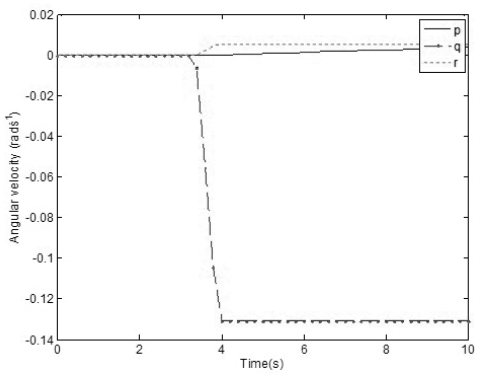


Figure 28. Trajectory plot during the excitation phase.

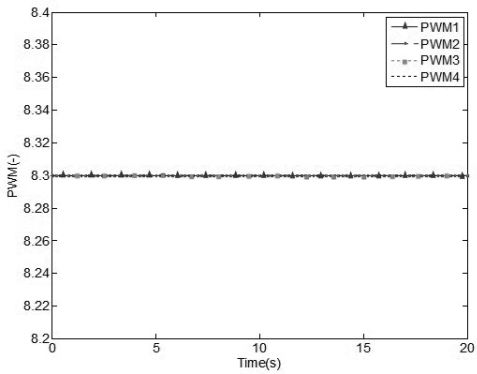


Figure 29. PWM input for the landing phase of the mission.

https://doi.org/10.1017/S0001924000010587 Published online by Cambridge University Press

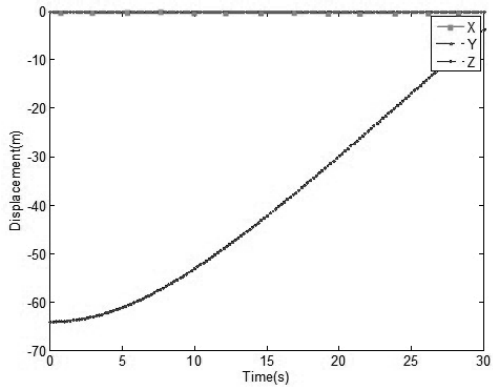


Figure 30. Variation in displacement with time during the descent phase.

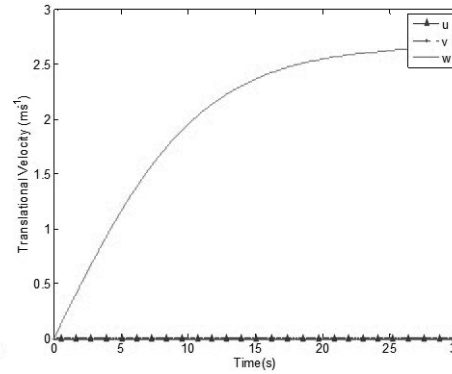


Figure 31. Variation in translational velocity with time during the descent phase.

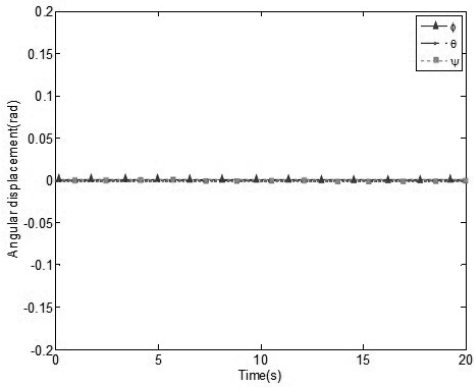


Figure 32. Variation in angular displacements with time during the descent phase.

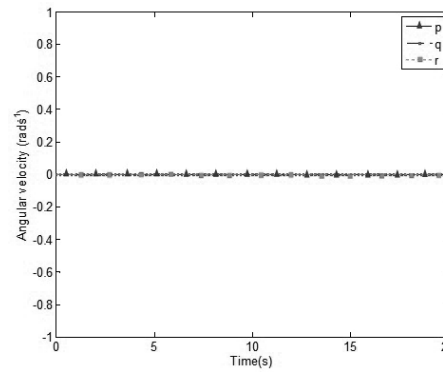


Figure 33. Variation in angular velocity with time during the descent phase.

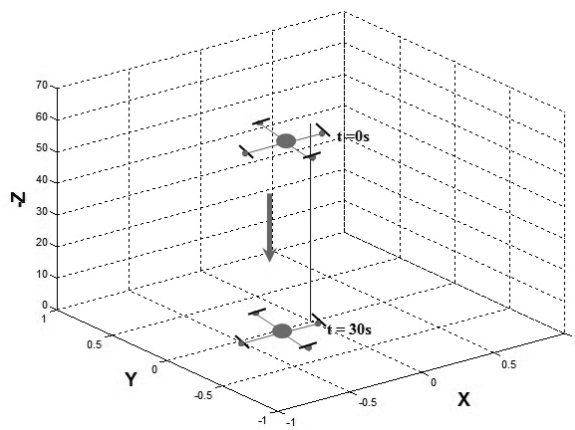


Figure 34. Trajectory plot during the descent phase.

https://doi.org/10.1017/S0001924000010587 Published online by Cambridge University Press

and velocity vector varies non linearly with time (see Fig. 30 and Fig. 31). During this phase level flight must be maintained which can be seen by the null angular displacement and velocity curves with time (see Fig. 32 and Fig. 33). The trajectory during this phase can be viewed in Fig. 34. It can be noted that lower PWM signal implies a smaller descent velocity and longer decent duration from its initial position.

8.0 CONCLUSION

The results of the data acquisition process had two main interests, that being the maximum thrust produced by a motor for the least amount of current and if the maximum allowable take-off weight with the chosen setup accommodates the simulation model mass. The 390KV motor combined with the 9 × 4·5″, 3 blade propeller produces the highest ratio of thrust to current but limitations imposed on the required model mass eliminated this setup. The 570KV motor with the 11 × 4·7″ propeller was selected due to the high efficiency and overhead to accommodate larger simulation model masses. The mathematical modelling was successfully realised using the graphical user interface of the Matlab environment. The initial model testing used the identified trends for the ascent, descent and hover phases as forms of model validation.

10.0 FUTURE WORK

Future work of the project will encompass the complete design and build of the quadrotor UAV with geometrical design features such as arm length and chassis geometry extracted from the mathematical model. A complete stress analysis will need to be conducted on the conceived chassis establishing areas prone to fatigue loading. Resonance was established to be one of the main design considerations noted by the rapid changes in displacement of the test beam and will be a design criteria. The preliminary design was built in order to facilitate a design space for the avionics and wiring and is a necessary pre-requisite. The absence of wind-tunnel test data for the purposes of quadrotor simulation makes drag estimation a tedious process. It remains an area that has not been explored and will be explored in the future. A custom built load cell will need to be built in order for the drag forces to be captured inside the wind-tunnel facilities adding a dynamic to the simulation that is missing in documented models.

REFERENCES

1. VACHTSEVANOS, G., LUDINGTON, B., REIMANN, J., ANTSAKLIS, P. and VALAVANIS, K. Modelling and Control of Unmanned Aerial Vehicles-Current Status and Future Directions, 2007, South Florida, USA, Workshop on Modelling and Control of Complex Systems.
2. DOMINGUES, J. Quadrotor Prototype, 2009, Master Thesis, University of Lisbon, Lisbon, Portugal.
3. SALIH, A., MOGHAVVEMI, M., MOHAMMED, H. and GAEID, K.S. Flight PID controller design for a UAV quadrotor, *Scientific Research Essays*, December 2010, **5**, (23), pp 3660-3667.
4. BHANDARI, S., RAHEJA, A., TANG, D., ORTEGA, K., GUITERREZ, A., ANDRADE, L., LUU, J., ROSE, M., YARALIAN, H. and LEUER, M. Modelling and Control of UAVs using Neural Networks. AIAA Modelling and Simulation Technologies Conference, 13-16 August 2012, Minneapolis, Minnesota, USA.
5. ACHTELIK, M., BIERLING,. WAN, J. and HÖCHT, L., 2011. Adaptive Control of a Quadcopter in the Presence of large/complete Parameter Uncertainties. Technical University of Munich, Munich, Germany.
6. ZAWISKI, R. and BLACHUTTA, M. Dynamics and Optimal Control of Quadrotor Platform. AIAA Guidance, Navigation and Control Conference, 2012, Minneapolis, Minnesota, USA.
7. GREMILLION, G. and HUMBER, J.S. 1-2 System Identification od a Quadrotor Micro Air Vehicle, August 2010, AIAA Atmospheric Flight Mechanics Conference, Toronto, Ontario, Canada.

https://doi.org/10.1017/S0001924000010587 Published online by Cambridge University Press

8. ALI RAZA, S. and ETELE, J. Simulation Tool for Testing and Validating Uav Autopilots in Wind Gust Environments. AIAA Atmospheric Flight Mechanics Conference, 13-16 August 2012, Minneapolis, Minnesota, USA.
9. STEPANIAK, M.J., VAN GRASS, F. and UIJT DE HAAG, M. Design of an electric propulsion system for a quadrotor unmanned aerial vehicle, *J Aircraft,* 3 May-June 2009, **46**, (3).
10. FINKPETERSON, C. *ET AL* Autonomous Hovering with a Quadrotor Helicopter, s.l., 2008, Aalrborg University.
11. CHERON, C., DENNIS, A. and SEMERJYAN, C,Y. A Multifunctional HIL Testbed for Multirotor VTOL UAV Actuator, Center for elf-Organizing and Intelligent Systems, Department of Electrical and Computer Engineering, 2010, Utah Sate University, USA.
12. POUNDS, P., MAHONY, R. and CORKE, P. System Identification and Control of an Aerobot Drive System, 2007, Department of Engineering, Austrailan National University, Austrailia.
13. HUANG, G., HOFFMAN, G., WASLANDER, S. and TOMLIN, C. Aerodymanics and Control of Autonomous Quadrotor Helicopters in Aggressive Maneuvering, IEEE International Conference on Robotics and Automation, 2009.
14. OLIVEIRA, M.D.L.C. d., 2011. Modelling, Identification and Cotrol of a Quadrotor Aircraft, Czech Technical University, Prague, Czech Republic.

https://doi.org/10.1017/S0001924000010587 Published online by Cambridge University Press